

## NMR relaxation induced by iron oxide particles: testing theoretical models

This content has been downloaded from IOPscience. Please scroll down to see the full text.

2016 Nanotechnology 27 155706

(<http://iopscience.iop.org/0957-4484/27/15/155706>)

View [the table of contents for this issue](#), or go to the [journal homepage](#) for more

Download details:

IP Address: 170.140.26.180

This content was downloaded on 12/03/2016 at 08:11

Please note that [terms and conditions apply](#).

# NMR relaxation induced by iron oxide particles: testing theoretical models

Y Gossuin<sup>1</sup>, T Orlando<sup>2</sup>, M Basini<sup>3,4</sup>, D Henrard<sup>1</sup>, A Lascialfari<sup>3</sup>, C Mattea<sup>5</sup>, S Stapf<sup>5</sup> and Q L Vuong<sup>1</sup>

<sup>1</sup> Biomedical Physics Department, University of Mons, 24, Avenue du Champ de Mars, B-7000, Mons, Belgium

<sup>2</sup> Department of Physics, University of Pavia, Via Bassi 6, I-27100 Pavia, Italy

<sup>3</sup> Department of Physics, Università degli studi di Milano and INSTM Unit, Via Celoria 16 I-20133 Milano, Italy

<sup>4</sup> CNR Nano S3 Via Campi 213/A, 41125 Modena, Italy

<sup>5</sup> Technische Universität Ilmenau, Fakultät für Mathematik und Naturwissenschaften, FG Technische Physik II/Polymerphysik, PO Box 100 565, D-98684 Ilmenau, Germany

E-mail: [yves.gossuin@umons.ac.be](mailto:yves.gossuin@umons.ac.be)

Received 19 October 2015, revised 25 January 2016

Accepted for publication 9 February 2016

Published 2 March 2016



CrossMark

## Abstract

Superparamagnetic iron oxide particles find their main application as contrast agents for cellular and molecular magnetic resonance imaging. The contrast they bring is due to the shortening of the transverse relaxation time  $T_2$  of water protons. In order to understand their influence on proton relaxation, different theoretical relaxation models have been developed, each of them presenting a certain validity domain, which depends on the particle characteristics and proton dynamics. The validation of these models is crucial since they allow for predicting the ideal particle characteristics for obtaining the best contrast but also because the fitting of  $T_1$  experimental data by the theory constitutes an interesting tool for the characterization of the nanoparticles. In this work,  $T_2$  of suspensions of iron oxide particles in different solvents and at different temperatures, corresponding to different proton diffusion properties, were measured and were compared to the three main theoretical models (the motional averaging regime, the static dephasing regime, and the partial refocusing model) with good qualitative agreement. However, a real quantitative agreement was not observed, probably because of the complexity of these nanoparticulate systems. The Roch theory, developed in the motional averaging regime (MAR), was also successfully used to fit  $T_1$  nuclear magnetic relaxation dispersion (NMRD) profiles, even outside the MAR validity range, and provided a good estimate of the particle size. On the other hand, the simultaneous fitting of  $T_1$  and  $T_2$  NMRD profiles by the theory was impossible, and this occurrence constitutes a clear limitation of the Roch model. Finally, the theory was shown to satisfactorily fit the deuterium  $T_1$  NMRD profile of superparamagnetic particle suspensions in heavy water.

 Online supplementary data available from [stacks.iop.org/NANO/27/155706/mmedia](http://stacks.iop.org/NANO/27/155706/mmedia)

Keywords: iron oxide particles, superparamagnetic particles, NMR relaxation theory, MRI contrast agent

(Some figures may appear in colour only in the online journal)

## Abbreviations

(NMR)	nuclear magnetic resonance
(MRI)	magnetic resonance imaging
(NMRD)	nuclear magnetic relaxation dispersion
(MAR)	motional averaging regime
(SDR)	static dephasing regime
(PRM)	partial refocusing regime

## Introduction

Iron oxide particles have been used for a long time as clinical magnetic resonance imaging (MRI) contrast agents, even if, now, they are mainly used in small animal imaging for cellular and molecular imagings [1]. These magnetic particles create contrast through their influence on the proton nuclear magnetic resonance (NMR) relaxation times  $T_1$  and  $T_2$ . Indeed, the dipolar coupling between their magnetic moments and the proton spins drastically quickens the relaxation of water protons [2]. This effect is more pronounced for transverse relaxation with a large shortening of  $T_2$ , except for very small particles that almost equally affect  $T_1$  and  $T_2$  at intermediate fields [3]. For larger particles, their marked effect on  $T_2$  makes them ideal negative contrast agents: their presence in a specific region of the body is accompanied by a loss of NMR signal, leading to dark areas on  $T_2$ -weighted MR images. Understanding the transverse relaxation mechanism is crucial since it allows for predicting which particles will be the most efficient. However, it also provides an original way to characterize the particles since their radii and saturation magnetizations can be determined by the fitting of the relaxation data with suited theoretical models.

Depending on the size of the particles and on their magnetization but also on the diffusion properties of the protons nearby the particles, different theoretical models have to be used for the description of the transverse relaxation at high magnetic fields, the so-called secular term of the relaxation equations. The motional averaging regime (MAR) must be applied when water protons experience a large variety of magnetic fields during the time of relaxation [4, 5]. On the other hand, if protons are almost static in the field inhomogeneities, the static dephasing regime (SDR) has to be used to predict  $T_2^*$  ( $T_2$  measured without refocusing pulses in the sequence). It also provides a good approximation for  $T_2$  as far as diffusion is fast enough to prevent the refocusing of the spins during the Car–Purcell–Meiboom–Gill (CPMG) sequence [6, 7]. In the opposite case, the partial refocusing model (PRM) [8] has to be used for  $T_2$ . All these models have been validated by numerical Monte Carlo simulations of transverse relaxation [8]. The agreement with the experimental data is relatively good, even if the comparison can be complicated by the size distribution of the particles, the influence of the coating of the iron oxide core, and the presence of clusters [9–12]. To test the different relaxation models, particles of different sizes and magnetizations can be

used [13–18]. The size of the particles is an important parameter for biomedical applications: these contrast agents often cluster in cellular culture and *in vivo*, which leads to the formation of larger ‘magnetic entities’ [19–23]. Therefore, a relaxation model valid in aqueous solutions with well dispersed particles fails to be a satisfactory approach to predict the behavior of the larger clusters often observed in cells [12, 21–23]. The same is true for the diffusion properties of water protons: diffusion can be up to three times slower in cells [24] than in aqueous solutions, which could also change the relaxation regime. Instead of changing the size of the particles to browse the relaxation models, we decided to use different solvents having proton diffusion coefficients that vary over almost four orders of magnitude but for a single type of particle. This allowed for traveling from MAR to PRM and for validating the models.

The aforementioned models provide estimations of  $T_2$  at high fields. However, in the MAR framework, a theoretical description of the relaxation induced by superparamagnetic particles possessing a uniaxial anisotropy has been proposed by Roch *et al* [4]. It allows predicting  $T_1$  and  $T_2$  at any magnetic field. This model has been validated through the fitting of  $T_1$  nuclear magnetic relaxation dispersion (NMRD) profiles that can be routinely obtained on a single fast field-cycling (FFC) relaxometer [25]. NMRD profiles represent the evolution of  $1/T_1$  with the magnetic field (the typical range for commercial FFC is from  $3.5 \times 10^{-4}$  to 1 T). The obtained curve is an invaluable tool to test the relaxation theories at all fields not only for high fields as is the case for  $T_2$  data from simulations or experiments, even if the values of the relaxivities measured at imaging fields are really important from the practical point of view [19, 20, 26, 27]. Moreover, the fitting of the NMRD profiles with the theory of Roch *et al* allows for obtaining the minimum approach distance of the solvent—which could be considered as the radius of the particle if the coating is perfectly permeable—and the saturation magnetization of the particles as well as the associated Néel relaxation time [28]. In this work,  $T_1$  NMRD profiles were measured for a large range of proton diffusion coefficients in order to test the validity domain of the well established Roch theory on a large field range. It is worth noting that, for particles presenting high anisotropy, as cobalt ferrites, another model has to be used [29].

Surprisingly,  $T_2$  measurements at high fields and  $T_1$  NMRD profiles are often (if not always) treated and are interpreted separately in literature. The characterization of new particles is usually carried out thanks to the fitting of the  $T_1$  NMRD profiles, and  $T_2$  is measured at a single magnetic field simply to evaluate the efficiency of the particles for biomedical applications without any comparison with a theoretical prediction of  $T_2$ . On the other hand, papers aimed at validating  $T_2$  relaxation theories with simulations or experiments are not using  $T_1$  NMRDs to refine their study [12, 14].  $T_2$  NMRD profiles are not easy to obtain with the FFC method since refocusing pulses are needed during the relaxation period. Moreover, the instability of the acquisition field can also affect the echo formation. Therefore, the experimental parameters of the measurements have to be

carefully chosen. The first  $T_2$  NMRD profiles of superparamagnetic particles covering a wide range of magnetic fields were published recently [30] but were not compared to the theoretical predictions of the relaxation models. Moreover, because of unwanted particle aggregation, the low field limit of  $T_1$  and  $T_2$  NMRD profiles reported in that study did not match as it should, however, be the case from a theoretical point of view. Indeed, the fundamental difference between  $T_1$  and  $T_2$  exist because of the presence of a finite magnetic field. At the zero field limit, they should be equal. In this work, we measured  $T_1$  and  $T_2$  NMRDs in the MAR regime and tested if they were simultaneously compatible with the predictions of Roch's model. This theory has also been applied with success to deuterium ( $^2\text{H}$ ) NMRD profiles of superparamagnetic particle suspensions.

## Materials and methods

### Samples

Some 3 nm very small iron oxide particles (VSOP3s) stabilized with sodium citrate were purchased from Ferropharm (Teltow, Germany). The iron concentration of the initial solution was 250 mM as determined by atomic emission spectroscopy after microwave digestion of the sample. The different solutions used for the NMR relaxation measurements were prepared with water, ethanol, dipropylene glycol, and a mixture of glycerol with 5%  $^2\text{H}$  oxide ( $^2\text{H}_2\text{O}$ ).  $^2\text{H}_2\text{O}$  was chosen in order to focus on the protons of glycerol. The volume weighted size and the saturation magnetization of the VSOP3 sample ( $R = 4.33$  nm and  $M_V = 330\,000$  A m $^{-1}$ ) were obtained from magnetometry by the fitting of the  $M-H$  curve at 300 K (obtained on a concentrated solution of particles) with a distribution of Langevin functions corresponding to a log-normal distribution of crystal sizes. VSOP3 particles were also dispersed in hexane after an exchange of ligand with oleic acid. Briefly, oleic acid was deprotonated with concentrated  $\text{NH}_4\text{OH}$  in a 1:1 molar ratio. The obtained emulsion was added to the aqueous suspension of particles under vigorous stirring in order to obtain a molar ratio of 5 between the total iron and the carboxylate groups of oleic acid. The formed magnetic paste was attracted with a magnet, the supernatant was removed, and, then, the magnetic paste was washed three times with methanol. Finally, hexane was added in order to obtain the dispersion of oleic acid coated particles in hexane. Dynamic light scattering (DLS) (Malvern Zetasizer) was used to measure the hydrodynamic size of the particles: the hydrodynamic diameter (volume weighted) is 10 nm in water, while it is about 22 nm in hexane due to the oleic acid coating.

Some 20 nm of VSOP20 stabilized with sodium citrate were also purchased from Ferropharm (Teltow, Germany). The iron concentration of the initial dispersion was 497 mM as determined by atomic emission spectroscopy after microwave digestion of the sample. The solution used for the  $^2\text{H}$  NMRD measurement was prepared with  $^2\text{H}_2\text{O}$  for a final proportion of  $^2\text{H}_2\text{O}$  versus normal water of 5:1. The volume

weighted size and the saturation magnetization ( $R = 4.82$  nm and  $M_V = 325\,000$  A m $^{-1}$ ) of the VSOP20 sample were obtained from magnetometry by the fitting of the  $M-H$  curve with a distribution of Langevin functions corresponding to a log-normal distribution of crystal sizes. The volume weighted hydrodynamic size of the VSOP20 particles was 26 nm.

### NMR measurements

$T_1$  NMRD profiles of the different suspensions were measured from 0.015 to 40 MHz with a Spinmaster FFC relaxometer (STELAR, Mede, Italy). The magnetic fields are expressed in units of proton Larmor frequency (except for figure 5 in order to ease the comparison between  $^1\text{H}$  and  $^2\text{H}$  data): a magnetic field of 1 T corresponds to a proton Larmor frequency of 42.6 MHz.  $T_2$  relaxation times were measured at 29, 20, and 60 MHz on a spintrack analyzer (Resonance Systems), a minispec mq20 relaxometer, and a minispec mq60 relaxometer (Bruker) by a CPMG sequence with an interecho time  $2\tau$  of 500  $\mu\text{s}$ .  $\tau$  is, thus, the echo time, i.e., the interval between the initial  $90^\circ$  pulse and the first  $180^\circ$  pulse. The hard radio frequency pulses used in this work were always shorter than 5  $\mu\text{s}$ . The relaxation occurring during the pulse can, therefore, be neglected. Variable temperature measurements were carried out at 29 MHz with a homemade temperature regulation controlled by a thermocouple with an accuracy of 0.5  $^\circ\text{C}$ .  $T_2$  NMRD profiles were acquired with a Smartracer FFC relaxometer (STELAR, Mede, Italy) using a spin echo sequence below 3 MHz and a CPMG sequence between 3 and 10 MHz (interecho time  $2\tau$  of 100  $\mu\text{s}$ ). Above 10 MHz, the  $T_2$  NMRD profile was measured with a LapNMR spectrometer (Tecmag) using a CPMG sequence (interecho time of  $2\tau = 500$   $\mu\text{s}$ ). The contribution of magnetic particles to the relaxation of glycerol  $^2\text{H}_2\text{O}$  mixtures was obtained after correction of the diamagnetic contribution from a 'blank' glycerol  $^2\text{H}_2\text{O}$  solution at the same temperature since the latter is not negligible under any circumstance. For other solvents, this correction was not necessary.

### Relaxation theories

Detailed descriptions of the different relaxation models can be found in literature [12, 14, 31]. However, the validity domains and final equations providing the relaxation rates will be rapidly recalled below. These models naturally employ important parameters reflecting the properties of the particles and the dynamics of protons, such as the equatorial Larmor frequency shift  $\Delta\omega$  and the diffusion correlation time  $\tau_D$ ,

$$\Delta\omega = \frac{\mu_0 \gamma M_V}{3}, \quad (1)$$

$$\tau_D = \frac{R^2}{D}, \quad (2)$$

where  $\mu_0$  is the vacuum magnetic permeability,  $\gamma$  is the proton gyromagnetic factor, and  $M_V$  is the single particle saturation magnetization of the particle expressed in the SI unit A m $^{-1}$ .  $R$  is the radius of the particle, and  $D$  is the proton diffusion

coefficient, equal to the diffusion coefficient of the molecule bearing protons. The interecho time  $2\tau$  of the CPMG sequence (defined as the time between two  $180^\circ$  pulses) used for the measurement of  $T_2$  also plays an important role in the transverse relaxation properties.  $f$  is the volume fraction of the particles, i.e., the ratio between the volume of the sample occupied by particles and the total sample volume. For pure magnetite particles, it is related to the iron concentration [13] by

$$f/[Fe] = v_{\text{mat}} = \frac{M_{\gamma\text{-Fe}_3\text{O}_4}}{2\rho_{\gamma\text{-Fe}_3\text{O}_4}} = 1.52 \times 10^{-5} \text{ m}^3 \text{ mol}^{-1}, \quad (3)$$

where  $\rho_{\gamma\text{-Fe}_3\text{O}_4} = 5100 \text{ kg m}^{-3}$  is the density of magnetite and  $M_{\gamma\text{-Fe}_3\text{O}_4}$  is the molar mass of magnetite in kg mol.

**MAR.** If  $\Delta\omega \tau_D \ll 1$ , the MAR must be applied. This condition, which can also be written as  $\tau_D \ll \frac{1}{\Delta\omega}$ , implies that protons experience a large range of magnetic fields during their diffusion in the neighboring of the particles. In that case, the transverse relaxation rate at high fields [5] is given by

$$R_2 = \frac{1}{T_2} = \frac{16}{45} f \tau_D (\Delta\omega)^2. \quad (4)$$

The general equations providing  $R_1$  and  $R_2$  for any value of the field [4] are as follows:

$$\begin{aligned} \frac{1}{T_1} = & \frac{8}{45} \tau_D \Delta\omega f \left[ 7P \frac{L(\xi)}{\xi} J_F(\omega_S, \tau_D, \tau_N) \right. \\ & \left. + \left[ 7(1-P) \frac{L(\xi)}{\xi} + 3 \left( 1 - 2 \frac{L(\xi)}{\xi} - L^2(\xi) \right) \right] \right] \quad (5) \\ & \times [J_F(\omega_I, \tau_D, \tau_N) + 3L^2(\xi) J_A(\omega_I, \tau_D)], \end{aligned}$$

$$\begin{aligned} \frac{1}{T_2^*} = & \frac{4}{45} \tau_D \Delta\omega f \left[ \frac{L(\xi)}{\xi} (13P J_F(\omega_S, \tau_D, \tau_N) \right. \\ & + 7(1-P) J_F(\omega_I, \tau_D, \tau_N) \\ & + 6(1-P) J_F(0, \tau_D, \tau_N)) \\ & + \left( 1 - 2 \frac{L(\xi)}{\xi} - L^2(\xi) \right) (3J_F(\omega_I, \tau_D, \tau_N) \\ & + 4J_F(0, \tau_D, \tau_N)) + L^2(\xi) (3J_A(\omega_I, \tau_D) \\ & \left. + 4J_A(0, \tau_D)) \right], \quad (6) \end{aligned}$$

$$J_F(\omega, \tau_D, \tau_N) = \text{Re} \left( \frac{1 + \frac{z^{1/2}}{4}}{1 + z^{1/2} + \frac{4z}{9} + \frac{z^{3/2}}{9}} \right)$$

with

$$z = \frac{\tau_D}{\tau_N} + \omega \tau_D i, \quad (7)$$

$$J_A(\omega, \tau_D) = \frac{1 + \frac{5z}{8} + \frac{z^2}{8}}{1 + z + \frac{z^2}{2} + \frac{z^3}{6} + \frac{4z^4}{81} + \frac{z^5}{81} + \frac{z^6}{648}}$$

with

$$z = \sqrt{2\omega\tau_D}, \quad (8)$$

where  $\omega_I$  and  $\omega_S$ , respectively, are the proton and the electron Larmor frequencies.  $\tau_N$  is the Néel relaxation time, and  $p$  is a fitting parameter composed between 0 and 1. These equations were used to fit the  $T_1$  NMRD profiles and to calculate the  $T_2$  NMRD profiles.

**SDR.** If the protons are perfectly static ( $\tau_D \rightarrow \infty$ ), the transverse relaxation rate at high fields measured without refocusing pulses  $R_2^*$ , is given [6] by

$$R_2^* = \frac{1}{T_2^*} = \frac{2\pi}{3\sqrt{3}} f \Delta\omega. \quad (9)$$

However, even for diffusing protons, this equation provides a good approximation of  $R_2$  if  $\tau_D > \frac{1}{\Delta\omega}$ . This approximation becomes more and more realistic as  $\tau_D$  increases.

The contribution of the magnetic particles to  $R_2$  (measured with a CPMG sequence) would be zero for perfectly static protons since the  $180^\circ$  pulses would completely refocus the spins dephased by the magnetic field inhomogeneities created by the particles. However, for diffusing protons,  $R_2$  can also be approximated by equation (9) when  $\frac{1}{\Delta\omega} < \tau_D < 2\tau$ ,  $2\tau$  being the interecho time of the CPMG sequence. The condition  $\tau_D < 2\tau$  prevents the refocusing of the dephased protons by the  $180^\circ$  pulses, which allows for approximating  $R_2$  by  $R_2^*$ .

**PRM.** When  $\frac{1}{\Delta\omega} < \tau_D$  with a CPMG interecho time of  $2\tau > \tau_D$ , the  $180^\circ$  pulses become effective, and  $R_2$  is smaller than the value of  $R_2^*$  given by equation (9). The PRM [8] allows for predicting the relaxation rate in this situation,

$$\begin{aligned} R_2 = \frac{1}{T_2} = & 2.25f \frac{x^{1/3}}{\tau_D} (1.34 + fx)^{5/3} \\ \text{with} & \\ x = & \sqrt{\frac{4}{5}} (\Delta\omega)\tau. \quad (10) \end{aligned}$$

Another theoretical model has been developed by Kurz *et al* [32] to predict  $T_2$  measured by a single spin echo experiment for large particles, but it cannot be directly applied to the case of CPMG sequences.

**Transition between models.** The transition between MAR and SDR regimes occurs when the condition  $R_2 = R_2^*$  from equations (4), (9), respectively, is fulfilled. The crossing point

is as follows:

$$\tau_D = \frac{R^2}{D} = \frac{5 \pi \sqrt{3}}{4 \Delta\omega}. \quad (11)$$

Similarly, equations (9), (10) allow for estimating when the PRM model should be used

$$\tau_D = \frac{R^2}{D} > \sqrt{\frac{5}{4}} \frac{1.66x^{1/3}(1.34 + fx)^{5/3}}{\Delta\omega}. \quad (12)$$

**Influence of the field on  $T_2$ .** Equations (4), (9), (10) provide an estimation of the transverse relaxation rate at high fields, namely, the secular term of equation (6). But what does high field mean in terms of relaxation models? The relaxation rate has already reached the secular term when the condition  $\gamma 2\pi B_0 \sim \frac{1}{\tau_D}$  is fulfilled [4]. For our samples, for the smaller values of  $\tau_D$ , it corresponds to a field of approximately 1 T. We can, thus, consider that the  $R_2$  values reported here would be valid at higher fields. It is worth noting that another effect of the field could appear if the magnetizations of the particles were not saturated. However, the saturation occurs below 0.25 T, which means that the magnetization of the particles is the same at all the fields above 0.25 T. The conclusions of this study should, thus, be applicable at higher fields.

### Proton diffusion coefficients

All the diffusion coefficients used in this work were found in literature or calculated thanks to interpolation of literature data. Water diffusion data were found in [33], glycerol water mixture diffusion coefficients were calculated from [34]. Ethanol data were found in [35], while dipropylene glycol diffusion coefficient was reported in [36]. Hexane diffusion data were found in [37]. An estimation of the  $^2\text{H}$  diffusion coefficient in a mixture of  $^2\text{H}_2\text{O}$  and water in a 5:1 proportion at 37 °C ( $D = 2.7 \text{ m}^2 \text{ s}^{-1}$ ) was used for the fitting of the  $^2\text{H}$  NMRD curve [38, 39].

### Results and discussion

Figure 1 shows the evolution of the transverse relaxation rate at 29 MHz for solutions of VSOP3 particles prepared with different solvents or mixtures of solvents and at different temperatures, always for the same volume fraction of nanoparticles. This allows for covering proton diffusion coefficients ranging from  $1.5 \times 10^{-12}$  to  $5 \times 10^{-9} \text{ m}^2 \text{ s}^{-1}$ . For glycerol  $^2\text{H}_2\text{O}$  mixtures, the diffusion coefficient of glycerol protons was used since  $^2\text{H}_2\text{O}$  molecules were silent for proton NMR. The evolution of transverse relaxation versus  $1/D$  is typical of what is reported in literature for particles of increasing radius. It is logical since the relevant parameter for the choice of a model is  $\tau_D = R^2/D$ . Increasing the radius or decreasing the diffusion coefficient both lead to an increase

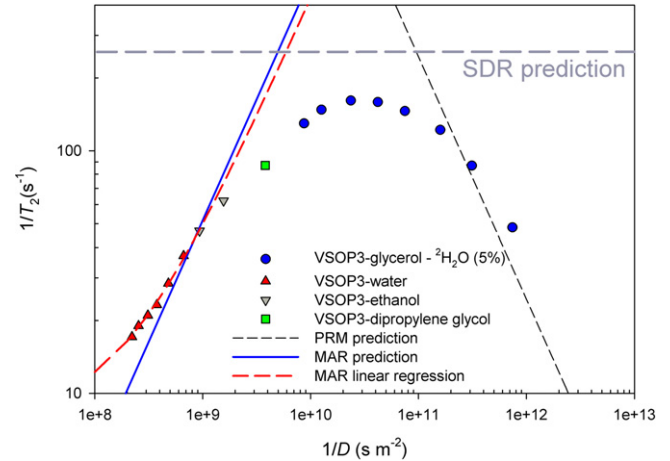


**Figure 1.** Evolution of the transverse relaxation rate at 29 MHz with the diffusion coefficient of protons for dispersions of VSOP3 particles.  $[\text{Fe}] = 0.37 \text{ mM}$  corresponding to  $f = 5.6 \times 10^{-6}$ . The MAR linear regression was performed with the data respecting the MAR condition.

in  $\tau_D$ . A first qualitative analysis of the results is rather straightforward: the left part of the data corresponds to the MAR with an increase in  $1/T_2$  for increasing  $1/D$ . The middle part corresponds to the static dephasing regime with a maximum of  $R_2$ . The following decrease in  $R_2$  for increasing  $1/D$  can be explained by the PRM. It is interesting to note that, for water at 37 °C, a decrease in the diffusion coefficient by a factor of 3 (as observed for water in cells) would lead to a 117% increase in the relaxation rate as illustrated by the data of water at different temperatures presented in figure 1.

Using the characteristics of the particles given in the materials and methods section ( $R = 4.33 \text{ nm}$  and  $Mv = 330\,000 \text{ A m}^{-1}$ ), one can calculate the theoretical predictions of the different models as well as their respective validity domains (equations (4)–(12)). Table 1 summarizes the results of these calculations.

When comparing the theoretical prediction of MAR with the fitting of the experimental data in the MAR domain, the slopes are clearly similar ( $5.16 \cdot 10^{-8}$  and  $4.2 \cdot 10^{-8} \text{ m}^2 \text{ s}^{-2}$ ). However, there is a major difference between the prediction and the data: we had to use an intercept in the regression of the  $R_2$  versus  $1/D$  data. The value of this intercept ( $8.05 \text{ s}^{-1}$ ) is far from negligible when compared to the relaxation rates that were measured. This does not seem justified from a theoretical point of view since the infinite diffusion coefficient should cancel the transverse relaxation in the MAR regime.  $2 \cdot 10^8 < 1/D < 1 \cdot 10^9$ . However, the perfect linear relationship (with a zero intercept) between  $R_2$  and  $1/D$  is only valid when speaking of the secular term of the relaxation equation. At 29 MHz,  $R_2$  could be slightly different from the secular term, and this difference will become larger for decreasing values of  $1/D$ . Indeed,  $R_2$  only reaches the secular term when the condition  $\gamma B_0 \frac{R^2}{D} \gg 1$  is fulfilled, which corresponds to a limit field of 25 MHz for water at 37 °C. But as  $1/D$  decreases, this limit field will increase. This could explain why our linear regression provides a non-null intercept. Figure S1 provides

**Table 1.** Validity domains of the different relaxation theories, theoretical predictions of the transverse relaxation rates, and their comparison with the experimental data.

	Validity domain	Prediction [Fe = 0.37 mM]— $f = 5.6 \times 10^{-6}$	Experimental value [Fe = 0.37 mM]— $f = 5.6 \times 10^{-6}$
MAR	$\Delta\omega \tau_D \ll 1$ $\Downarrow$ $1/D \ll 1.4 \times 10^9 \text{ s m}^{-2}$	$R_2 = 5.16 \times 10^{-8} \frac{1}{D}$  Blue curve	$R_2 = a \frac{1}{D} + b$  with $a = (4.2 \pm 0.11) \times 10^{-8}$ $b = 8.05 \pm 0.41$ Red curve, linear regression of data corresponding to $1/D < 1.4 \times 10^9 \text{ s m}^{-2}$ $R_2 \approx 160 \text{ s}^{-1}$
SDR	$1/D > 4.76 \times 10^9 \text{ s m}^{-2}$ and $1/D < 9.04 \times 10^{10} \text{ s m}^{-2}$	$R_2 = 258 \text{ s}^{-1}$ gray curve	
PRM	$1/D \gg 9.04 \times 10^{10} \text{ s m}^{-2}$	For $2\tau = 500 \mu\text{s}$ $R_2 = 2.37 \times 10^{13} D$ Black curve	Not enough data

the results of the exact calculation of  $R_2$  at 29 MHz using equation (6) for different values of  $1/D$ . It shows that a non-null intercept could be obtained when considering  $R_2$  at 29 MHz for intermediate values of  $1/D$ .

In the SDR domain, the maximum of relaxation is clearly observed, even if the measured value of this maximum is smaller ( $160 \text{ s}^{-1}$ ) than the predicted one ( $258 \text{ s}^{-1}$ ). This can be understood by taking the size distribution of the particles into account: as already shown by Carroll *et al* [14], all the particles of the samples will not fall in the SDR. Some larger particles will be in the PRM regime, while some other ones will still be in the MAR. Since the MAR and PRM predictions are always smaller than the SDR one, this could explain the difference between the theoretical SDR value and the measured one. Finally, in the PRM region, the prediction seems coherent with the experimental points, even if a real comparison is difficult due to the lack of experimental data for very high  $1/D$  values. The  $T_2$  relaxation data, thus, seem in qualitative agreement with the predictions of the secular term provided by the three models of transverse relaxation.

To evaluate a possible influence of the solvent, another test was carried out with the same particles but was dispersed in hexane after their coating with oleic acid. The  $T_2$  data in hexane solutions at different temperatures are in qualitative agreement with the MAR predictions calculated for the corresponding values of diffusion coefficients (figure 2). For a 5.45 mM solution, the regression of the data gives

$$R_2^{\text{exp}} = 12.1 \times 10^{-7} \frac{1}{D} - 24.$$

The negative intercept ( $-24 \text{ s}^{-1}$ ) obtained by the linear regression of the data may seem large, but it has less impact than in the case of aqueous solutions because the measured relaxation rates were rather large because high iron concentrations were used.

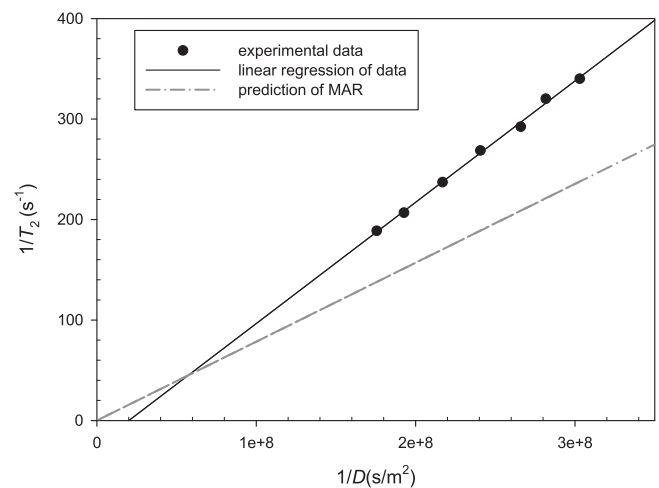


**Figure 2.** Evolution of the transverse relaxation rate with the diffusion coefficient of protons for hexane suspensions of VSOP3 particles. [Fe] = 5.45 mM corresponding to  $f = 8.3 \times 10^{-5}$ . Only the data respecting the MAR condition are shown.

The MAR prediction calculated with the particle characteristics ( $Mv = 330\,000$ ,  $R = 4.33 \text{ nm}$ ) is as follows:

$$R_2^{\text{theo}} = 7.6 \times 10^{-7} \frac{1}{D}.$$

However, this prediction does not take into account the existence of the oleic acid layer, which is supposed to prevent water molecules from getting close to the crystal.

Since the Roch model (using the MAR framework) allows the calculation of  $T_1$  at any field,  $T_1$  NMRD were measured for particles in different solvents and at different temperatures and, then, were fitted by the theory. Figure 3 shows the NMRD profiles of different samples corresponding to different diffusion coefficients. Table 2 shows the parameters obtained from the fitting as well as the corresponding values of  $\Delta\omega \tau_D$  in order to identify the samples for which the theoretical model is valid. In particular, only four samples

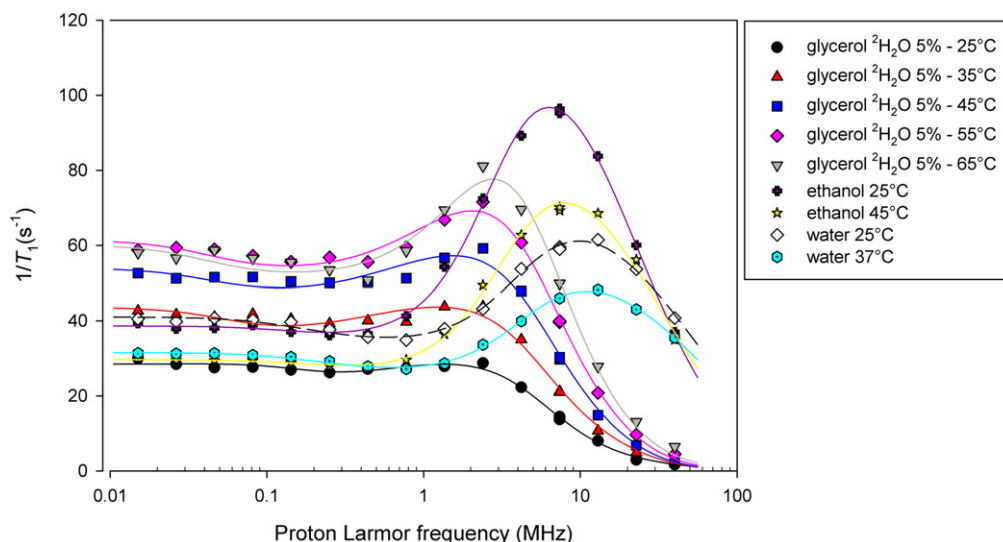


**Figure 3.**  $T_1$  NMRD profiles of dispersions of VSOP3 particles in different solvents and at different temperatures.  $[Fe] = 1.49$  mM, corresponding to  $f = 2.26 \times 10^{-5}$ . Lines are best fits of the data with the model of Roch *et al* [4].

**Table 2.** Parameters obtained from the fitting of the NMRD profiles of solutions of VSOP3 particles in different solvents and at different temperatures<sup>6</sup>.

VSOP3 particle solvent and temperature	$R$ (nm)	$M_v$ ( $A\ m^{-1}$ )	Néel relaxation time (ns)	$p$	$\Delta\omega\ \tau_D$	$D$ ( $10^{-9}\ m^2\ s^{-1}$ )
Water 25 °C	$4.19 \pm 0.05$	$316\ 000 \pm 3600$	$2.71 \pm 0.09$	$0.25 \pm 0.026$	0.31	2.3
Water 37 °C	$4.25 \pm 0.03$	$308\ 000 \pm 2200$	$2.26 \pm 0.046$	$0.25 \pm 0.015$	0.27	3
Ethanol 25 °C	$4.93 \pm 0.037$	$269\ 000 \pm 1800$	$2.1 \pm 0.05$	$0.13 \pm 0.04$	0.67	1.07
Ethanol 45 °C	$4.82 \pm 0.06$	$273\ 000 \pm 3100$	$1.67 \pm 0.06$	$0.15 \pm 0.06$	0.44	1.63
Glycerol $^2H_2O$ 5% 25 °C	$4.3 \pm 0.15$	$232\ 000 \pm 19000$	$1.39 \pm 0.24$	$0.57 \pm 0.11$	187	0.0038
Glycerol $^2H_2O$ 5% 35 °C	$4.95 \pm 0.13$	$166\ 000 \pm 14000$	$4.24 \pm 0.7$	$0.25 \pm 0.07$	88	0.0081
Glycerol $^2H_2O$ 5% 45 °C	$4.99 \pm 0.09$	$162\ 000 \pm 8000$	$5.57 \pm 0.6$	$0.18 \pm 0.06$	45	0.0157
Glycerol $^2H_2O$ 5% 55 °C	$4.95 \pm 0.07$	$171\ 000 \pm 4300$	$5.77 \pm 0.30$	$0.2 \pm 0.044$	25	0.0284
Glycerol $^2H_2O$ 5% 65 °C	$5.28 \pm 0.11$	$166\ 000 \pm 4000$	$6.42 \pm 0.37$	$0.2 \pm 0.07$	9	0.078
Hexane 25 °C	$6.26 \pm 0.10$	$172\ 000 \pm 1500$	$0.79 \pm 0.04$	$0.02 \pm 0.09$	0.09	4.15
VSOP20 particles	$R$ (nm)	$M_v$ ( $A\ m^{-1}$ )	Néel relaxation time (ns)	$p$	$\Delta\omega\ \tau_D$	$D$ ( $10^{-9}\ m^2\ s^{-1}$ )
Proton NMRD, 37 °C	$6.49 \pm 0.12$	$234\ 000 \pm 3700$	$1.88 \pm 0.11$	$0.0 \pm 0.21$	0.28	3
$^2H$ NMRD, 37 °C	$6.16 \pm 0.28$	$329\ 000 \pm 16000$	$1.19 \pm 0.19$	$0.0 \pm 0.27$	0.043	2.7

obey the condition  $\Delta\omega\ \tau_D < 1$ . This means that, strictly speaking, the MAR can only be applied for these four samples. However, the NMRD curves of all other samples with  $\Delta\omega\ \tau_D > 1$ , can be fitted by the model that provides rather good estimations of the radius, even if the magnetization is always underestimated. This shows that the fitting of NMRD profiles remains a good tool for the estimation of the distance of minimum approach (= crystal radius for a permeable coating), even beyond the validity domain of the model of Roch *et al*, i.e., the MAR conditions that could finally be too restrictive. A similar strategy was used by Kruk *et al* [40] to measure the diffusion coefficient of decalin and toluene at different temperatures through the fitting of the NMRD profiles of magnetic particles in these solvents. However, the theoretical approach used in this study is different from ours

since it is based on the theory of Kellar *et al* [41], which does not take the anisotropy into account [5].

While equation (4) only provides the secular term of transverse relaxation corresponding to the high field limit, the Roch model also predicts  $T_2$  for any value of the field. Therefore, another simple check of the consistency of the model would consist of the measurement of both  $T_1$  and  $T_2$  NMRD profiles and a simultaneous fitting of both profiles. Such a fitting was impossible to achieve. Therefore, after the usual fitting of the  $T_1$  NMRD profile, the measured  $T_2$  NMRD profile was simply compared with the predicted  $T_2$  NMRD profile, calculated using the parameters obtained from the fitting of the  $T_1$  profile. Figure 4(a) shows the  $T_1$  and  $T_2$  NMRD profiles of the nanoparticles in water at 25 °C. Clearly, the predictions of  $T_2$  are not in agreement with the

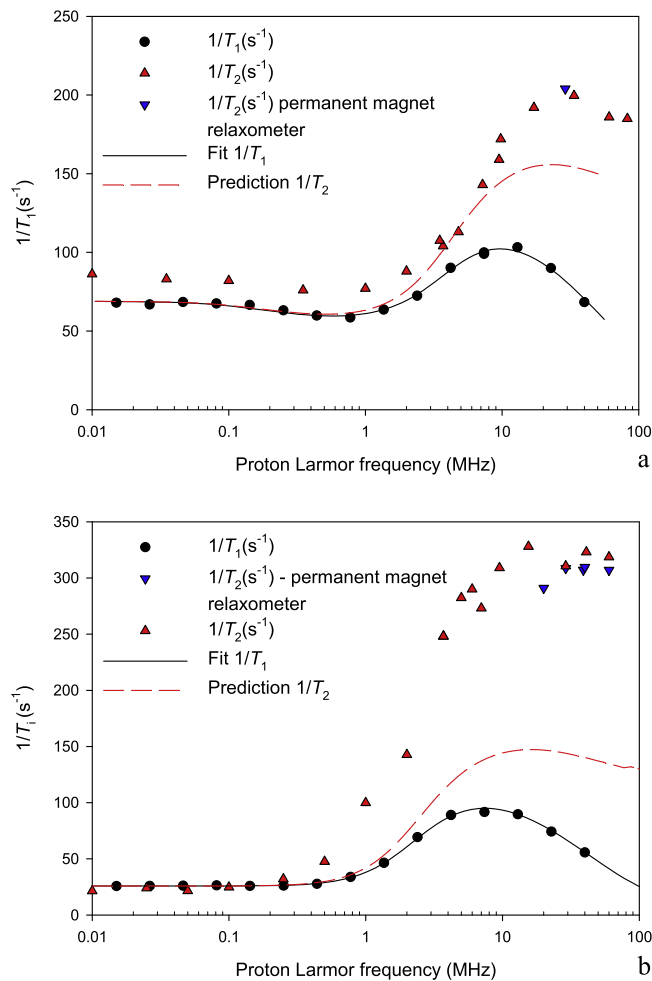


**Figure 4.**  $T_1$  and  $T_2$  NMRD profiles of VSOP3 particles suspensions in water (a) and hexane (b) at 25 °C.  $[\text{Fe}] = 2.5$  mM, corresponding to  $f = 3.8 \times 10^{-5}$ . The black line represents the fit of the  $T_1$  data by the Roch model. The red curve represents the prediction of  $T_2$  provided by the Roch model using the parameters obtained from the  $T_1$  fitting.

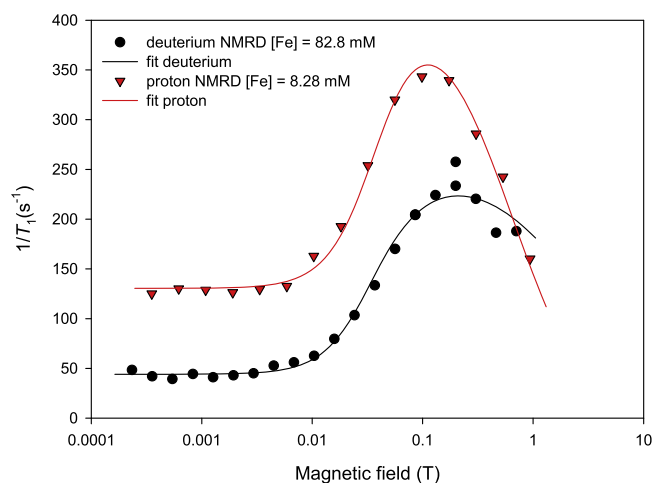


**Figure 5.** Proton and  $^2\text{H}$   $T_1$  NMRD profiles of suspensions of VSOP20 particles at 37 °C. The iron concentration of the aqueous solution of VSOP20 particles was 8.28 mM (corresponding to  $f = 1.29 \times 10^{-4}$ ), while the concentration of the dispersion of VSOP20 in  $^2\text{H}_2\text{O}$  was 82.8 mM (corresponding to  $f = 1.29 \times 10^{-3}$ ).

experimental data for frequencies  $>6$  MHz.  $T_1$  and  $T_2$  NMRD profiles were also measured and were compared for VSOP3 particles dispersed in hexane (figure 4(b)): the differences between predicted and experimental  $T_2$  NMRD profiles are even worse than for the aqueous solution. In both cases, experimental  $1/T_2$  larger than predicted  $1/T_2$  were obtained. This discrepancy explains why a simultaneous fitting of  $T_1$  and  $T_2$  NMRD profiles is impossible, while it could have been an option to refine the characterization of the particles. This limitation of the model can have several origins as the influence of the size distribution of the particles or the presence of clusters in the samples. The coating of the particles and the diffusion properties of water in the coating (if it is permeable) are also not taken into account in the theory: in particular, the existence of a first coordination sphere around the particle where water protons stay for longer times with respect to  $\tau_D$  could be considered. Indeed, the surface of the particles, when accessible, is far from inert: it is covered by hydroxyl groups and bound water molecules, which is not included in the model, while it has been shown to be the cause of relaxation for hydrated iron oxide nanoparticles [42].

To our knowledge, Roch's theory has never been used for nuclei other than protons. However, it is also possible to record NMRD profiles for  $^2\text{H}$ . This nucleus may not seem to be the best candidate for such a test of the superparamagnetic theory: the latter is based on the dipolar interaction between the particle and the nucleus, while  $^2\text{H}$  is known to relax mainly through quadrupolar interaction. However, in the case of superparamagnetic particles, the moment of the particle is so enormous that the dipolar interaction between the  $^2\text{H}$  and the particle dominates the relaxation as illustrated in figure 5, which presents the  $^1\text{H}$  and  $^2\text{H}$  NMRD profiles of VSOP 20 nm particles. The  $^2\text{H}$  NMRD presents the typical shape obtained for superparamagnetic particles, especially the increase in the relaxation rate at intermediate fields that correspond to the increase in the magnetic moment of the particle and the subsequent maximum before the dispersion due to the more important role of diffusion. After the adaptation of the relevant parameters in the Roch equations, we fitted this  $^2\text{H}$  NMRD profile and compared the results with those obtained from the fitting of the proton NMRD profile of the same sample (table 2). The agreement between the data extracted from the  $^1\text{H}$  and  $^2\text{H}$  NMRDs is relatively good, which seems to prove that the theory of Roch *et al* can also be used to describe the longitudinal relaxation of other nuclei diffusing in the presence of superparamagnetic particles when the dipolar interaction between the particle and the nuclear spin is the origin of relaxation.

One could question the applicability of these models *in vivo* or in iron oxide loaded cells where iron oxide particles form large clusters on the micrometer scale. However, it is possible to use the theories presented in this work to evaluate qualitatively the relaxation induced by suspensions of cells loaded with iron oxide particles. For example, in the study of Klug *et al* [20] on macrophages loaded with VSOP C200 particles (similar to those used in our study), the relaxivity of an iron loaded cell suspension is  $32 \text{ s}^{-1} \text{ mM}^{-1}$ , while it was  $79 \text{ s}^{-1} \text{ mM}^{-1}$  for the same particles in aqueous suspension.

This decrease in relaxivity could be understood thanks to the relaxation models: in aqueous suspensions, the particles are in the MAR, and their relaxivity is really close to the relaxivity obtained in this study for VSOP3 particles ( $r_2^{\text{cell}} = 76 \text{ s}^{-1} \text{ mM}^{-1}$ ). However, when clustered inside cells, the relaxation model can change from MAR to PRM. However, if we try to estimate  $r_2$  considering the cell like a large but less magnetized particle, the agreement is not obvious:  $r_2^{\text{cell}} = 95.6 \text{ s}^{-1} \text{ mM}^{-1}$ . All the details of this calculation are provided in the supplementary material. The same result is obtained when considering only a single aggregate of iron oxide particles (present in each cell), neglecting the presence of the cellular membrane:  $r_2^{\text{cluster}} = 98 \text{ s}^{-1} \text{ mM}^{-1}$ , see the supplementary material for details. This proves that iron loaded cell suspensions have to be considered as more complex systems, and that relaxation theories must be used carefully. However, in some cases, the qualitative agreement is good. Wuerfel *et al* [19] reported a drastic decrease in the relaxivity of VSOPC200 particles when internalized into T cells ( $r_2 = 4.23 \text{ s}^{-1} \text{ mM}^{-1}$ ). Again, an estimation of  $r_2$  can be obtained with equation (10). If we consider the cell like an impenetrable less magnetized particle,  $r_2^{\text{cell}} = 11 \text{ s}^{-1} \text{ mM}^{-1}$ , while if we only consider a single cluster in each cell, neglecting the membrane,  $r_2^{\text{cluster}} = 11.2 \text{ s}^{-1} \text{ mM}^{-1}$  (see supplementary material for calculation details). In this case, the PRM theory predicts the observed decrease in  $r_2$  after the internalization of particles into cells. The case of the suspensions of loaded cells is, in fact, not so realistic: most of the water (99%) is outside the cell for a volume fraction of cells of 1%, and, therefore, most of the signal arises from these water protons that present almost the same diffusion coefficient as free water. It is true, even when cells are trapped in agarose gels since the microscopic diffusion of water is not decreased much in a 2% gel [43]. However, in tissue, extracellular space only represents 20% of the total volume. This means that intracellular water has to be taken into account with its specific diffusion properties and the effect of the membrane permeability. The hindered diffusion [44] of extracellular water around the cellular structure will also influence the relaxation induced by the presence of iron oxide into the cells. This could possibly be taken into account by introducing an apparent diffusion coefficient and a tortuosity parameter. Moreover, the compartmentalization of protons often leads to multiexponential relaxation, which is difficult to describe with simple theoretical models.

In this work, the three relaxation theories predicting the secular term of transverse relaxation induced by iron oxide particles—namely, the MAR, the SDR, and the PRM—and their validity domains were tested thanks to relaxometry experiments on magnetic particles dispersed in different solvents and at different temperatures, which allowed for changing the proton diffusion coefficient on almost four orders of magnitude. The results are in qualitative agreement with the different theories, even if some unexplained discrepancies were observed.

It was possible to fit the  $T_1$  NMRD profiles of the different samples with the Roch theory, even outside its validity domain, which provided a rather good estimation of the radius

of the particles (for a permeable coating). NMRD profiles, thus, remain a good characterization tool for the particles, even outside the MAR. When the experimental  $T_2$  NMRD profiles were compared to the prediction of the Roch theory, the agreement was poor with an underestimation of experimental  $1/T_2$  values. This could be related to some missing mechanism in theory, which has a fundamental role in  $T_2$  relaxation. Finally, the theory was used successfully to describe the  $^2\text{H}$  relaxation induced by superparamagnetic particles, which proves that, in this case, the dipolar interaction is so strong that  $^2\text{H}$  does not relax through the quadrupolar interaction as is usually the case.

## Conclusion

The final conclusion of this study is twofold: on one hand, the theories were shown to describe qualitatively the relaxation induced by superparamagnetic particles in a large range of diffusion coefficients and even for  $^2\text{H}$  relaxation in the presence of superparamagnetic particles. However, a fully quantitative description of the relaxation by the current models seems difficult to achieve because they do not take into account all the characteristics of the particles as their size distributions and surface properties. Moreover, the application of the models to iron oxide loaded cells and tissues is not straightforward because of the complexity of these systems.

## Acknowledgments

YG acknowledges L Vander Elst for access to the low field FFC and DLS devices. This work was partially funded by FRS-FNRS. YG warmly thanks B Chen for providing the data for the calculation of the glycerol diffusion coefficients.

## References

- [1] Bulte J W M and Kraitchman D L 2004 Iron oxide MR contrast agents for molecular and cellular imaging *NMR Biomed.* **17** 484–99
- [2] Gossuin Y, Gillis P, Hocq A, Vuong Q L and Roch A 2009 Magnetic resonance relaxation properties of superparamagnetic particles *Interdiscip. Rev. Nanomed. Nanobiotechnol.* **1** 299–310
- [3] Sandiford L *et al* 2013 Bisphosphonate-anchored PEGylation and radiolabeling of superparamagnetic iron oxide: long-circulating nanoparticles for *in vivo* multimodal (T1 MRI-SPECT) imaging *ACS Nano* **7** 500–12
- [4] Roch A, Muller R N and Gillis P 1999 Theory of proton relaxation induced by superparamagnetic particles *J. Chem. Phys.* **110** 5403–11
- [5] Gillis P, Roch A and Brooks R A 1999 Corrected equations for susceptibility-induced T2-shortening *J. Magn. Reson.* **137** 402–7
- [6] Brown R J S 1961 Distribution of fields from randomly placed dipoles: free-precession signal decay as result of magnetic grains *Phys. Rev.* **121** 1379–82

- [7] Yablonskiy D A and Haacke E M 1994 Theory of NMR signal behavior in magnetically inhomogeneous tissues: the static dephasing regime *Magn. Reson. Med.* **32** 749–63
- [8] Gillis P, Moïny F and Brooks R A 2002 On T<sub>2</sub>-shortening by strongly magnetized spheres: a partial refocusing model *Magn. Reson. Med.* **47** 257–63
- [9] LaConte L E W, Nitin N, Zurkiya O, Caruntu D, O'Connor C J, Hu X and Bao G 2007 Coating thickness of magnetic iron oxide nanoparticles affects R<sub>2</sub> relaxivity *J. Magn. Reson. Imaging* **26** 1634–41
- [10] Carroll M R J, Huffstetler P P, Miles W C, Goff J D, Davis R M, Riffle J S, House M J, Woodward R C and St Pierre T G 2011 The effect of polymer coatings on proton transverse relaxivities of aqueous suspensions of magnetic nanoparticles *Nanotechnology* **22** 325702
- [11] Roch A, Gossuin Y, Muller R N and Gillis P 2005 Superparamagnetic colloid suspensions: water magnetic relaxation and clustering *J. Magn. Magn. Mater.* **293** 532–9
- [12] Vuong Q L, Gillis P and Gossuin Y 2011 Monte Carlo simulation and theory of proton NMR transverse relaxation induced by aggregation of magnetic particles used as MRI contrast agents *J. Magn. Reson.* **212** 139–48
- [13] Vuong Q L, Berret J-F, Fresnais J, Gossuin Y and Sandre O 2012 A universal scaling law to predict the efficiency of magnetic nanoparticles as MRI T<sub>2</sub>-contrast agents *Adv. Healthc. Mater.* **1** 502–12
- [14] Carroll M R J, Woodward R C, House M J, Teoh W Y, Amal R, Hanley T L and St Pierre T G 2010 Experimental validation of proton transverse relaxivity models for superparamagnetic nanoparticle MRI contrast agents *Nanotechnology* **21** 035103
- [15] Weisskoff R, Zuo C S, Boxerman J L and Rosen B R 1994 Microscopic susceptibility variation and transverse relaxation: theory and experiment *Magn. Reson. Med.* **31** 601–10
- [16] Pothayee N, Balasubramaniam S, Pothayee N, Jain N, Hu N, Lin Y, Davis R M, Sriranganathan N, Koretsky A P and Riffle J S 2013 Magnetic nanoclusters with hydrophilic spacing for dual drug delivery and sensitive magnetic resonance imaging *J. Mater. Chem. B* **1** 1142
- [17] Lartigue L, Hugouenq P, Alloyeau D, Clarke S P, Lévy M, Bacri J-C, Bazzi R, Brougham D F, Wilhelm C and Gazeau F 2012 Cooperative organization in iron oxide multi-core nanoparticles potentiates their efficiency as heating mediators and MRI contrast agents *ACS Nano* **6** 10935–49
- [18] Xie X and Zhang C 2011 Controllable assembly of hydrophobic superparamagnetic iron oxide nanoparticle with mPEG-PLA copolymer and its effect on MR transverse relaxation rate *J. Nanomater.* **2011** 1–7
- [19] Wuerfel E 2011 Electrostatically stabilized magnetic nanoparticles—an optimized protocol to label murine T cells for *in vivo* MRI *Front. Neurol.* **2** 72
- [20] Klug G *et al* 2010 Intracellular and extracellular T<sub>1</sub> and T<sub>2</sub> relaxivities of magneto-optical nanoparticles at experimental high fields *Magn. Reson. Med.* **64** 1607–15
- [21] Lévy M, Wilhelm C, Devaud M, Levitz P and Gazeau F 2012 How cellular processing of superparamagnetic nanoparticles affects their magnetic behavior and NMR relaxivity: magnetic and nmr behaviors of cell-processed USPIO *Contrast Media Mol. Imaging* **7** 373–83
- [22] Billotey C, Wilhelm C, Devaud M, Bacri J C, Bittoun J and Gazeau F 2003 Cell internalization of anionic maghemite nanoparticles: Quantitative effect on magnetic resonance imaging *Magn. Reson. Med.* **49** 646–54
- [23] Orlando T *et al* 2014 NMR as evaluation strategy for cellular uptake of nanoparticles *Nano Lett.* **14** 3959–65
- [24] Åslund I and Topgaard D 2009 Determination of the self-diffusion coefficient of intracellular water using PGSE NMR with variable gradient pulse length *J. Magn. Reson.* **201** 250–4
- [25] Kimmich R and Anorado E 2004 Field-cycling NMR relaxometry *Prog. Nucl. Magn. Reson. Spectrosc.* **44** 257–320
- [26] Gharagouzloo C A, McMahon P N and Sridhar S 2015 Quantitative contrast-enhanced MRI with superparamagnetic nanoparticles using ultrashort time-to-echo pulse sequences: QUTE-CE MRI with ferumoxytol *Magn. Reson. Med.* **74** 431–41
- [27] Wang L, Corum C A, Idiyatullin D, Garwood M and Zhao Q 2013 T<sub>1</sub> estimation for aqueous iron oxide nanoparticle suspensions using a variable flip angle SWIFT sequence: T<sub>1</sub> quantification of SPIO nanoparticles *Magn. Reson. Med.* **70** 341–7
- [28] Bordonali L *et al* 2013 NMR-D study of the local spin dynamics and magnetic anisotropy in different nearly monodispersed ferrite nanoparticles *J. Phys.: Condens. Matter* **25** 066008
- [29] Lévy M, Gazeau F, Wilhelm C, Neveu S, Devaud M and Levitz P 2013 Revisiting MRI contrast properties of nanoparticles: beyond the superparamagnetic regime *J. Phys. Chem. C* **117** 15369–74
- [30] Arosio P *et al* 2013 Hybrid iron oxide-copolymer micelles and vesicles as contrast agents for MRI: impact of the nanostructure on the relaxometric properties *J. Mater. Chem. B* **1** 5317
- [31] Laurent S, Forge D, Port M, Roch A, Robic C, Vander Elst L and Muller R N 2008 Magnetic iron oxide nanoparticles: synthesis, stabilization, vectorization, physicochemical characterizations, and biological applications *Chem. Rev.* **108** 2064–110
- [32] Kurz F T, Kampf T, Heiland S, Bendszus M, Schlemmer H-P and Ziener C H 2014 Theoretical model of the single spin-echo relaxation time for spherical magnetic perturbers *Magn. Reson. Med.* **71** 1888–95
- [33] Holz M, Heil S R and Sacco A 2000 Temperature-dependent self-diffusion coefficients of water and six selected molecular liquids for calibration in accurate <sup>1</sup>H NMR PFG measurements *Phys. Chem. Chem. Phys.* **2** 4740–2
- [34] Chen C, Li W Z, Song Y C, Weng L D and Zhang N 2012 Concentration dependence of water self-diffusion coefficients in dilute glycerol–water binary and glycerol–water–sodium chloride ternary solutions and the insights from hydrogen bonds *Mol. Phys.* **110** 283–91
- [35] Guevara-Carrion G, Nieto-Draghi C, Vrabc J and Hasse H 2008 Prediction of transport properties by molecular simulation: methanol and ethanol and their mixture *J. Phys. Chem. B* **112** 16664–74
- [36] Wang M-H, Soriano A N, Caparanga A R and Li M-H 2010 Binary mutual diffusion coefficient of aqueous solutions of propylene glycol and dipropylene glycol *J. Taiwan Inst. Chem. Eng.* **41** 279–85
- [37] Harris K R 1982 Temperature and density dependence of the self-diffusion coefficient of n-hexane from 223 to 333 K and up to 400 MPa *J. Chem. Soc. Faraday Trans. 1* **78** 2265–74
- [38] Mills R 1973 Self-diffusion in normal and heavy water in the range 1–45 deg *J. Phys. Chem.* **77** 685–8
- [39] Longworth L G 1960 The mutual diffusion of light and heavy water *J. Phys. Chem.* **64** 1914–7
- [40] Kruk D, Korpała A, Taheri S M, Kozłowski A, Förster S and Rössler E A 2014 <sup>1</sup>H relaxation enhancement induced by nanoparticles in solutions: influence of magnetic properties and diffusion *J. Chem. Phys.* **140** 174504

- [41] Koenig S H and Kellar K E 1995 Theory of  $1/T_1$  and  $1/T_2$  NMRD profiles of solutions of magnetic nanoparticles *Magn. Reson. Med.* **34** 227–33
- [42] Gossuin Y, Roch A, Muller R N and Gillis P 2000 Relaxation induced by ferritin and ferritin-like magnetic particles: the role of proton exchange *Magn. Reson. Med.* **43** 237–43
- [43] Davies E, Huang Y, Harper J B, Hook J M, Thomas D S, Burgar I M and Lillford P J 2010 Dynamics of water in agar gels studied using low and high resolution  $^1\text{H}$  NMR spectroscopy *Int. J. Food Sci. Technol.* **45** 2502–7
- [44] Sykova E and Nicholson C 2008 Diffusion in brain extracellular space *Physiol. Rev.* **88** 1277–340